

Itinerant in-plane magnetic fluctuations and many-body correlations in Na_xCoO_2

M.M. Korshunov ^{1,2} *, I. Eremin ^{2,3}, A. Shorikov ⁴, V.I. Anisimov ⁴, M. Renner ³, and W. Brenig ³

¹ *L.V. Kirensky Institute of Physics, Siberian Branch of Russian Academy of Sciences, 660036 Krasnoyarsk, Russia*

² *Max-Planck-Institut für Physik komplexer Systeme, D-01187 Dresden, Germany*

³ *Institute für Mathematische und Theoretische Physik,
TU Braunschweig, 38106 Braunschweig, Germany* and

⁴ *Institute of Metal Physics, Russian Academy of Sciences-Ural Division, 620041 Yekaterinburg GSP-170, Russia*

(Dated: April 2, 2018)

Based on the *ab-initio* band structure for Na_xCoO_2 we derive the single-electron energies and the effective tight-binding description for the t_{2g} bands using projection procedure. Due to the presence of the next-nearest-neighbor hoppings a local minimum in the electronic dispersion close to the Γ point of the first Brillouin zone forms. Correspondingly, in addition to a large Fermi surface an electron pocket close to the Γ point emerges at high doping concentrations. The latter yields the new scattering channel resulting in a peak structure of the itinerant magnetic susceptibility at small momenta. This indicates dominant itinerant in-plane ferromagnetic fluctuations above certain critical concentration x_m , in agreement with neutron scattering data. Below x_m the magnetic susceptibility shows a tendency towards the antiferromagnetic fluctuations. We further analyze the many-body effects on the electronic and magnetic excitations using various approximations applicable for different U/t ratio.

PACS numbers: 74.70.-b; 71.10.-w; 75.40.Cx; 31.15.Ar

I. INTRODUCTION

The recent discovery of the superconductivity in hydrated lamellar cobaltate $\text{Na}_x\text{CoO}_2 \cdot y\text{H}_2\text{O}$ ¹ raised tremendous interest in the nature and symmetry of the superconductive pairing in these materials. The phase diagram of this compound, with varying electron doping concentration x and water intercalation y , is rich and complicated; in addition to superconductivity, it exhibits magnetic and charge orders, and some other structural transitions^{2,3,4,5}. The parent compound, Na_xCoO_2 , is a quasi-two-dimensional system with Co in CoO_2 layers forming a triangular lattice where the Co-Co in-plane distance is two times smaller than the inter-plane one. Na ions reside between the CoO_2 layers and donate additional x electrons to the layer, lowering the Co valence from Co^{4+} ($3d^5$ configuration) to Co^{3+} ($3d^6$ configuration) upon changing x from 0 (CoO_2) to 1 (NaCoO_2). The hole in the d -orbital occupies one of the t_{2g} levels, which are lower than e_g levels by about 2 eV⁶. The degeneracy of the t_{2g} levels is partially lifted by the trigonal crystal field distortion which splits the former into the higher lying a_{1g} singlet and the lower two e'_g states.

First principles LDA (local density approximation) and LDA+U band structure calculations predict Na_xCoO_2 to have a large Fermi surface (FS) centered around the $\Gamma = (0, 0, 0)$ point with mainly a_{1g} character and six hole pockets near the $\text{K} = (0, \frac{4\pi}{3}, 0)$ points of the hexagonal Brillouin zone of mostly e'_g character for a wide range of x ^{6,7}. At the same time, recent surface sensitive Angle-Resolved Photo-Emission Spectroscopy (ARPES) experiments^{8,9,10,11} reveals a doping dependent evolution of the Fermi surface, which shows no sign of hole pockets for a wide range of Na concentrations, i.e. $(0.3 \leq x \leq 0.8)$. Instead, the Fermi surface is observed to be cen-

tered around the Γ point and to have mostly a_{1g} character. Furthermore, a dispersion of the valence band is measured which is only half of that calculated within the LDA. This indicates the importance of the electronic correlations in Na_xCoO_2 .

Shubnikov-de Haas effect measurements revealed two well-defined frequencies in $\text{Na}_{0.3}\text{CoO}_2$, suggesting either the existence of Na superstructures or the presence of the e'_g pockets¹². Last possibility was found to be incompatible with existing specific heat data. Also, within the LDA scheme the Na disorder was shown to destroy the small e'_g pockets in $\text{Na}_{2/3}\text{CoO}_2$ because of their tendency towards the localization¹³.

The hole pockets are absent in the LSDA+U (Local Spin Density Approximation + Hubbard U) calculations¹⁴. However, in this approach the insulating gap is formed by a splitting of the local single-electron states due to spin polarization, resulting in a spin polarized Fermi surface with an area twice as larger as ARPES observes.

The dynamical character of the strong electron correlations has been taken into account within Dynamical Mean Field Theory (DMFT) calculations¹⁵ and, surprisingly has led to an enhancement of the area of the small Fermi surface pockets, in contrast to the experimental observations. At the same time, the use of the strong-coupling Gutzwiller approximation within the multiorbital Hubbard model with fitting parameters¹⁶ yields an absence of the hole pockets at the Fermi surface. According to these findings, the bands crossing the Fermi surface have a_{1g} character.

Concerning the magnetic properties, LSDA predicts Na_xCoO_2 to have a weak intra-plane itinerant ferromagnetic (FM) state for nearly all Na concentrations, $0.3 \leq x \leq 0.7$ ¹⁷. On contrary, neutron scattering

finds A-type antiferromagnetic order at $T_m \approx 22$ K with an inter(intra)-plane exchange constant $J_{c(ab)} = 12(-6)$ meV and with ferromagnetic ordering within Co-layer *only* for $0.75 \leq x \leq 0.9$ ^{18,19,20}.

In this paper we derive an effective low-energy model describing the bands crossing the Fermi level on the basis of the LDA band structure calculations. Due to the FS topology, inferred from LDA band structure, the magnetic susceptibility $\chi_0(\mathbf{q}, \omega = 0)$ reveals two different regimes. For $x < 0.56$ the susceptibility shows pronounced peaks at the antiferromagnetic (AFM) wave vector $\mathbf{Q}_{AFM} = \left\{ \left(\frac{2\pi}{3}, \frac{2\pi}{\sqrt{3}} \right), \left(\frac{4\pi}{3}, 0 \right) \right\}$ resulting in a tendency towards in-plane 120° AFM order. For $x > 0.56$ the susceptibility is peaked at small momenta near $\mathbf{Q}_{FM} = (0, 0)$. This clearly demonstrates the tendency of the system towards an itinerant in-plane FM state. We find that the formation of the electron pocket around the Γ point is crucial for the in-plane FM ordering at high doping concentrations. We further analyze the role of the many-body effects calculated within the Fluctuation-Exchange (FLEX), Gutzwiller, and Hubbard-I approximations.

The paper is organized as follows. In Section II the LDA band structure and tight-binding model parameters derivation are described. The doping dependent evolution of the magnetic susceptibility within the tight-binding model is presented in Section III. The role of strong electron correlations is analyzed in Section IV. The last Section summarizes our study.

II. TIGHT-BINDING MODEL

The band structure of $\text{Na}_{0.61}\text{CoO}_2$ was obtained within the LDA²¹ in the framework of TB-LMTO-ASA (Tight Binding approach to the Linear Muffin-Tin-Orbitals using Atomic Sphere Approximation)²² computation scheme. This compound crystallizes at 12K in the hexagonal structure ($P6_3/mmc$ symmetry group) with $a=2.83176\text{\AA}$ and $c=10.84312\text{\AA}$ ²³. A displacement of Na atoms from its ideal sites $2d$ ($1/3, 2/3, 3/4$) on about 0.2\AA are observed in defected cobaltates for both room and low temperatures. This is probably due to the repulsion of the randomly distributed Na atoms, locally violating hexagonal symmetry²³. In this study Na atoms were shifted back to the high symmetry $2d$ sites. Oxygen was situated in the high-symmetry $2d$ -position ($1/2, 2/3, 3/4$). The obtained Co-O distance is 1.9066\AA which agrees well with experimentally observed one $1.9072(4)\text{\AA}$ ²³. This unit cell was used for all doping concentrations. The effect of the doping was taken into account within the virtual crystal approximation where each Co site has six nearest neighbor virtual atoms with fractional number of valence electrons x and a core charge $10 + x$ instead of randomly located Na. Note, that all core states of the virtual atom are left unchanged and corresponds to Na ones. We have chosen Co $4s, 4p, 3d$

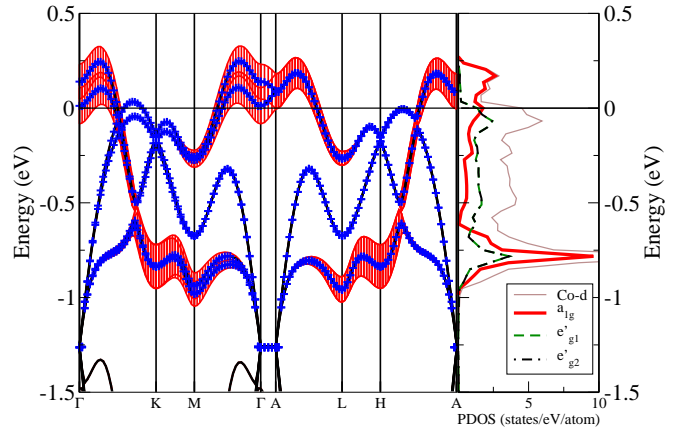


FIG. 1: (color online) Calculated near-Fermi level LDA band structure and partial density of states (PDOS) for $\text{Na}_{0.33}\text{CoO}_2$. The contribution of Co- a_{1g} states is denoted by the vertical broadening (in red) of the bands with thickness proportional to the weight of the contribution. The crosses indicate the dispersion of the bands obtained by projection on the t_{2g} orbitals. The horizontal line at zero energy denotes the Fermi level.

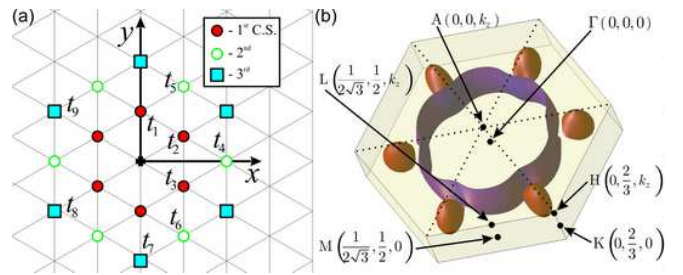


FIG. 2: (color online) (a) Schematic crystal structure of the Co-layer in Na_xCoO_2 with hopping notations within the first three coordination spheres (C.S.). (b) LDA-calculated Fermi surface with cylindrical part (violet) having mostly a_{1g} character and six hole pockets (red) having mostly e'_g character. k_x and k_y coordinates of the symmetry points are given in units of $2\pi/a$ with a being the in-plane lattice constant.

states, $2s, 2p, 3d$ states of O and $3s, 3p, 3d$ states of Na as the valence states for the TB-LMTO-ASA computation scheme. The radii of atomic spheres are 1.99 a.u. for Co, 1.61 a.u. for oxygen, and 2.68 a.u. for Na. Two classes of empty spheres (pseudo-atoms without core states) were added in order to fill the unit cell volume.

In order to find an appropriate basis the occupation matrix was diagonalized and its eigenfunctions were used as the new local orbitals. This procedure takes into account the real distortion of the crystal structure. The new orbitals are not pure trigonal a_{1g} and e'_g orbitals but we still use the former notations for the sake of simplicity. 288 k -points in the whole Brillouin zone were used for the band structure calculations (12x12x2 mesh for k_x , k_y , and k_z , correspondingly).

The bands crossing the Fermi level are shown in (Fig. 1). One sees that they have mostly a_{1g} character,

consistent with previous LDA findings⁶. Note, the small FS pockets near the K point with e'_g -symmetry present at $x = 0.33$ [see Fig. 2(b)] disappear for higher doping concentrations because of the corresponding bands sink below the Fermi level. The difference in the dispersion along K – M and L – H directions is due to non-negligible interaction between CoO₂ planes. A small gap between Co-3d and O-2p states at about -1.25 eV present for $x=0.61$ disappears for $x=0.33$ due to the shift of the *d*-band to lower energy upon decreasing number of electrons.

In the following we restrict ourselves to the model with the in-plane hoppings inside CoO₂ layer to describe the doping dependence of the itinerant in-plane magnetic order. Hence we neglect bonding-antibonding (bilayer) splitting present in the LDA-bands. This assumption seems to be justified since the largest interlayer hopping matrix element is an order of magnitude smaller than the intra-plane one (0.012 eV vs. 0.12 eV).

To construct the effective Hamiltonian and to derive the effective Co-Co hopping integrals $t_{fg}^{\alpha\beta}$ for the t_{2g} -manifold we apply the projection procedure^{24,25}. Here, $(\alpha\beta)$ denotes a pair of orbitals, a_{1g} , e'_{g1} or e'_{g2} . The indices *f* and *g* correspond to the Co-sites on the triangular lattice. The obtained hoppings and the single-electron energies are given in Table I for three difference doping concentrations. A comparison between the bands obtained using projection procedure and the LDA bands is shown in Fig. 1 confirming the Co- t_{2g} nature of the near-Fermi level bands^{6,26}. For simplicity we have enumerated site pairs with $n = 0, 1, 2, \dots$, $t_{fg}^{\alpha\beta} \rightarrow t_n^{\alpha\beta}$ (see Fig. 2(a) and the correspondence between in-plane vectors and index *n* in Table I). Due to the C_3 symmetry of the lattice, the following equalities apply: $|t_3^{\alpha\beta}| = |t_1^{\alpha\beta}|$, $|t_5^{\alpha\beta}| = |t_4^{\alpha\beta}|$, $|t_9^{\alpha\beta}| = |t_7^{\alpha\beta}|$. In addition $t_1^{\alpha\beta} = t_2^{\alpha\beta}$ for $a_{1g} \rightarrow a_{1g}$ hoppings, which, however, does not hold for $e'_{g1,2}$ orbitals. Since the hybridization between the a_{1g} and the e'_g bands is not small, a simplified description of the bands crossing the Fermi level in terms of the a_{1g} band only (neglecting e'_g band and the corresponding hybridizations, see for example Ref.²⁷) may lead to an incorrect result due to a higher symmetry of the a_{1g} -band.

In summary, the free electron Hamiltonian for CoO₂-plane in a hole representation is given by:

$$H_0 = - \sum_{\mathbf{k}, \alpha, \sigma} (\varepsilon^\alpha - \mu) n_{\mathbf{k}\alpha\sigma} - \sum_{\mathbf{k}, \sigma} \sum_{\alpha, \beta} t_{\mathbf{k}}^{\alpha\beta} d_{\mathbf{k}\alpha\sigma}^\dagger d_{\mathbf{k}\beta\sigma}. \quad (1)$$

where $d_{\mathbf{k}\alpha\sigma}$ ($d_{\mathbf{k}\alpha\sigma}^\dagger$) is the annihilation (creation) operator for the hole with momentum \mathbf{k} , spin σ and orbital index α , $n_{\mathbf{k}\alpha\sigma} = d_{\mathbf{k}\alpha\sigma}^\dagger d_{\mathbf{k}\alpha\sigma}$, and $t_{\mathbf{k}}^{\alpha\beta}$ is the Fourier transform of the hopping matrix element, ε^α is the single-electron energies, and μ is the chemical potential. Introducing matrix notations, $(\hat{t}_{\mathbf{k}})_{\alpha\beta} = t_{\mathbf{k}}^{\alpha\beta}$ and $(\hat{t}_n)_{\alpha\beta} = t_n^{\alpha\beta}$, the hoppings matrix elements in the momentum representa-

tion are given by:

$$\begin{aligned} \hat{t}_{\mathbf{k}} = & 2\hat{t}_1 \cos k_2 + 2\hat{t}_2 \cos k_3 + 2\hat{t}_3 \cos k_1 \\ & + 2\hat{t}_4 \cos(k_1 + k_3) + 2\hat{t}_5 \cos(k_2 + k_1) + 2\hat{t}_6 \cos(k_1 - k_2) \\ & + 2\hat{t}_7 \cos 2k_2 + 2\hat{t}_8 \cos 2k_3 + 2\hat{t}_9 \cos 2k_1, \end{aligned} \quad (2)$$

$$\text{where } k_1 = \frac{\sqrt{3}}{2}k_x - \frac{1}{2}k_y, k_2 = k_y, k_3 = \frac{\sqrt{3}}{2}k_x + \frac{1}{2}k_y.$$

Note, the parameters do not change significantly upon changing the doping concentration. In Fig. 3 we show two results of the rigid-band approximation with the Hamiltonian (1) and the hopping values obtained in LDA calculation for two different doping concentrations, $x = 0.33$ and $x = 0.61$ (see Table I). The doping concentration used to calculate the chemical potential μ was fixed to be $x = 0.61$ for both Hamiltonians. Although one finds the pronounced differences in the dispersion around the M-point, they are small around the FS. Since most of the physical quantities are determined by the states lying close to the Fermi level, we can safely ignore the small differences of the band structure and describe the doping evolution of the Na_xCoO₂ by simply varying the chemical potential. In the following we will use *ab initio* parameters calculated for $x = 0.33$ and change the chemical potential to achieve different doping concentrations.

Within the rigid band approximation the e'_g hole pockets are well below the Fermi level for $x \geq 0.41$. Most important however, we find the local minimum of the band dispersion around the Γ point (see Fig. 3) to yield an inner FS contour centered around this point. The area of this electron FS pocket increases upon increasing the doping concentration x . As we will show later, the main reason for the local minimum around the Γ point is the presence of the next-nearest-neighbor hopping integrals which enter our tight-binding dispersion. Although this minimum is not yet directly observed by ARPES experiments, note that the inner FS contour would reduce the total FS volume and therefore may explain why the volume of the FS observed in ARPES so far is larger than it follows from Luttinger's theorem²⁸. Furthermore, an emergence of this pocket would influence the Hall conductivity at high doping concentrations which is interesting to check experimentally.

Note, the appearance of the inner contour of the FS around the Γ point for large doping concentrations is not unique to our calculations, previously it has been obtained within the LDA calculations for a single Co-layer per unit cell¹⁴.

III. MAGNETIC SUSCEPTIBILITY

To analyze the possibility of the itinerant magnetism we calculate the magnetic susceptibility $\chi_0(\mathbf{q}, \omega = 0)$ based on the Hamiltonian H_0 . The doping-dependent evolution of the peaks in $\text{Re}\chi_0(\mathbf{q}, 0)$ is shown in Fig. 4. At $x = 0.41$ the e'_g bands are below the Fermi level, and the FS has the form of the rounded hexagon. It results in

TABLE I: Single-electron energies ϵ^α (relative to $\epsilon^{a_{1g}}$) and in-plane hopping integrals $t_n^{\alpha\beta}$ for Na_xCoO_2 , where $x = 0.33, 0.61, 0.7$. (all values are in eV)

		in-plane vector:	$(0, 1)$	$(\frac{\sqrt{3}}{2}, \frac{1}{2})$	$(\frac{\sqrt{3}}{2}, -\frac{1}{2})$	$(\sqrt{3}, 0)$	$(\frac{\sqrt{3}}{2}, \frac{3}{2})$	$(\frac{\sqrt{3}}{2}, -\frac{3}{2})$	$(0, 2)$	$(\sqrt{3}, 1)$	$(\sqrt{3}, -1)$
α	ϵ^α	$\alpha \rightarrow \beta$	$t_1^{\alpha\beta}$	$t_2^{\alpha\beta}$	$t_3^{\alpha\beta}$	$t_4^{\alpha\beta}$	$t_5^{\alpha\beta}$	$t_6^{\alpha\beta}$	$t_7^{\alpha\beta}$	$t_8^{\alpha\beta}$	$t_9^{\alpha\beta}$
$x = 0.33$											
a_{1g}	0.000	$a_{1g} \rightarrow a_{1g}$	0.123	0.123	0.123	-0.022	-0.022	-0.021	-0.025	-0.025	-0.025
		$a_{1g} \rightarrow e'_{g1}$	-0.044	0.089	-0.044	0.010	0.010	-0.021	-0.021	0.042	-0.021
e'_{g1}	-0.053	$a_{1g} \rightarrow e'_{g2}$	-0.077	0.000	0.077	0.018	-0.018	0.000	-0.036	0.000	0.036
		$e'_{g1} \rightarrow e'_{g1}$	-0.069	-0.005	-0.069	0.018	0.018	-0.026	-0.017	-0.085	-0.017
e'_{g2}	-0.053	$e'_{g1} \rightarrow e'_{g2}$	0.037	0.000	-0.037	-0.026	0.026	0.000	-0.039	0.000	0.039
		$e'_{g2} \rightarrow e'_{g2}$	-0.026	-0.090	-0.027	-0.011	-0.011	0.033	-0.062	0.006	-0.062
$x = 0.61$											
a_{1g}	0.000	$a_{1g} \rightarrow a_{1g}$	0.110	0.110	0.110	-0.019	-0.019	-0.019	-0.023	-0.023	-0.023
		$a_{1g} \rightarrow e'_{g1}$	-0.050	0.100	-0.050	0.008	0.008	-0.016	-0.017	0.035	-0.017
e'_{g1}	-0.028	$a_{1g} \rightarrow e'_{g2}$	0.087	0.000	-0.087	-0.014	0.014	0.000	0.030	-0.000	-0.030
		$e'_{g1} \rightarrow e'_{g1}$	-0.069	-0.031	-0.069	0.015	0.015	-0.022	-0.016	-0.076	-0.016
e'_{g2}	-0.028	$e'_{g1} \rightarrow e'_{g2}$	-0.022	0.000	0.022	0.021	-0.021	0.000	0.035	0.000	-0.035
		$e'_{g2} \rightarrow e'_{g2}$	-0.044	-0.081	-0.044	-0.009	-0.009	0.027	-0.056	0.005	-0.056
$x = 0.7$											
a_{1g}	0.000	$a_{1g} \rightarrow a_{1g}$	0.105	0.105	0.105	-0.018	-0.018	-0.018	-0.022	-0.022	-0.022
		$a_{1g} \rightarrow e'_{g1}$	-0.052	0.104	-0.052	0.007	0.007	-0.015	-0.016	0.033	-0.016
e'_{g1}	-0.019	$a_{1g} \rightarrow e'_{g2}$	-0.090	0.000	-0.090	0.013	-0.013	0.000	-0.028	0.000	0.028
		$e'_{g1} \rightarrow e'_{g1}$	-0.068	-0.039	-0.068	0.014	0.014	-0.020	-0.015	-0.073	-0.015
e'_{g2}	-0.019	$e'_{g1} \rightarrow e'_{g2}$	0.016	0.000	-0.016	-0.020	0.020	0.000	-0.034	0.000	0.034
		$e'_{g2} \rightarrow e'_{g2}$	-0.048	-0.077	-0.049	-0.009	-0.009	0.026	-0.054	0.005	-0.054

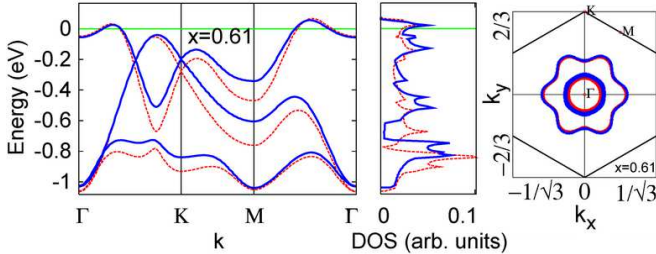


FIG. 3: (color online) Calculated tight-binding energy dispersion, the density of states (DOS), and the Fermi surface for $\text{Na}_{0.61}\text{CoO}_2$ within the rigid-band approximation with *ab initio* parameters for $x = 0.61$ (the solid blue curve) and for $x = 0.33$ (red dashed curve). The horizontal (green) line denotes the chemical potential μ for $x = 0.61$.

a number of nesting wave vectors around the antiferromagnetic wave vector \mathbf{Q}_{AFM} . The corresponding broad peaks in the $\text{Re}\chi_0(\mathbf{q}, 0)$ appear around \mathbf{Q}_{AFM} , indicating the tendency of the electronic system towards an 120° AFM SDW ordered state²⁹. Upon increasing doping, the Fermi level crosses the local minimum at the Γ point, resulting in an almost circle inner FS contour. As soon as this change of the FS topology occurs, the scattering at the momentum \mathbf{Q}_{AFM} is strongly suppressed at $x_m \geq 0.56$. Simultaneously, a new scattering vector, \mathbf{Q}_1 , at small momenta appears. Correspondingly, the magnetic susceptibility peaks at small momenta, indicating the tendency of the magnetic system towards itinerant SDW order with small momenta. The relevance of the

local minimum around the Γ point for the formation of the scattering at small momenta was originally found in Ref.²⁷.

For large x the area of the inner FS contour increases leading to a further decrease of the \mathbf{Q}_1 . Observe that for $x \approx 0.88$, the FS topology again changes yielding six distant FS contours that moves \mathbf{Q}_1 further to zero momenta. The scattering at small momenta seen in the bare magnetic susceptibility for $x > x_m$ is qualitatively consistent with the ferromagnetic ordering at $\mathbf{Q}_{FM} = (0, 0)$, observed in the neutron scattering experiments^{18,19,20}.

IV. EFFECTS OF STRONG ELECTRON CORRELATIONS

It is important to understand the impact of electronic correlations on the magnetic instabilities obtained within the rigid band approximation. Since obtained magnetic susceptibility depends mostly on the topology of the FS one expects that the behavior shown in Fig. 4 will be valid even if one consider an RPA susceptibility with an interaction term H_{int} taken into account, at least in the case if the only interaction is the on-site Hubbard repulsion U . The only difference would be a shift of the critical concentrations x_m , at which the FS topology changes and tendency to the AFM order changes towards the tendency to the FM ordered state. Similar to Refs.^{16,30} we add the on-site Coulomb interaction terms to Eq.(1). At present, it is not completely clear to which extent the electronic correlations governs the low-energy properties

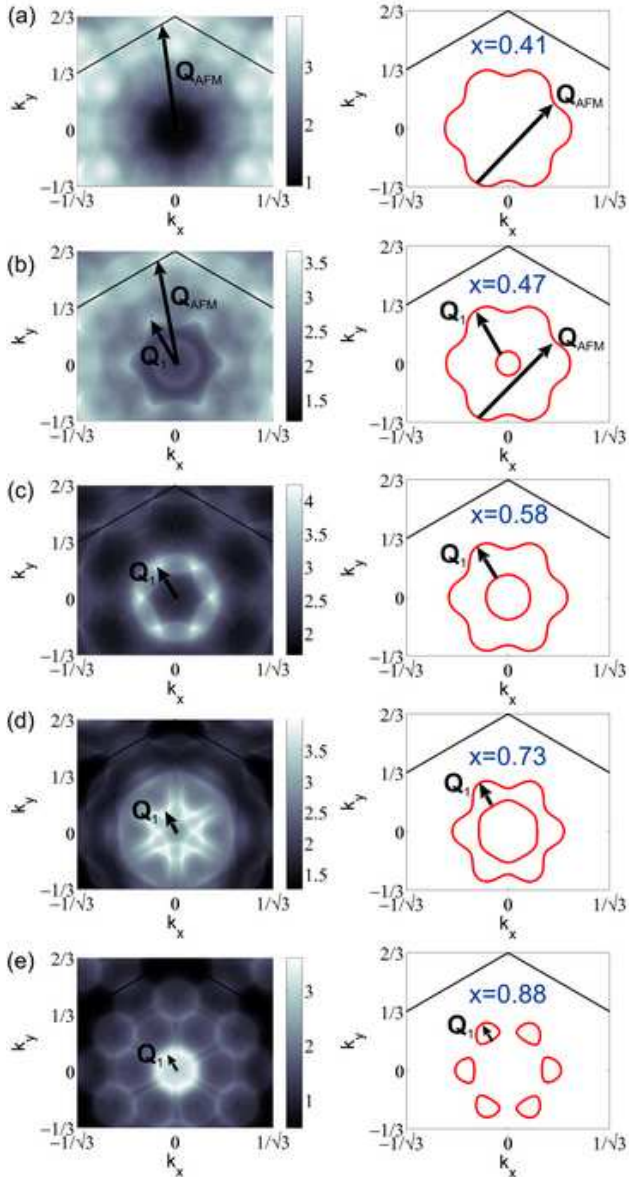


FIG. 4: (color online) The contour plot of the real part of the magnetic susceptibility $\text{Re}\chi_0(\mathbf{k}, \omega = 0)$ as a function of the momentum in units of $2\pi/a$ (left), and the Fermi surface for corresponding doping concentration x (right). The arrows indicate the scattering wave vectors \mathbf{Q}_i as described in the text.

in Na_xCoO_2 due to multi-orbital effects in this compound which complicates the situation. Therefore, in the following we discuss three different approximations valid for different U/t ratio.

A. Hubbard-I approximation

To analyze the regime of strong electron correlations we project the doubly occupied states out and formulate an effective model equivalent to the Hubbard model with

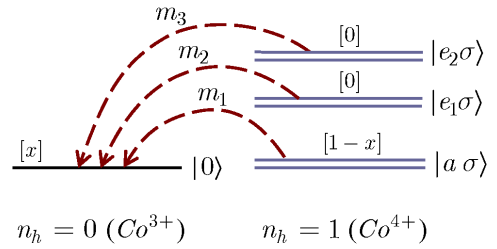


FIG. 5: (color online) A schematic picture of the local atomic states on Co and the single-particle excitations in Na_xCoO_2 . Here n_h stands for number of holes, m_i enumerates single-particle excitations. The filling factor of the corresponding state upon changing the doping concentration x is given in square brackets.

an infinite value of U . This approximation could be justified by the large ratio of the on-site Coulomb interaction on the CoO_2 cluster U with respect to the bandwidth W . In the atomic limit the local low-energy states on the Co sites are the vacuum state $|0\rangle$ and the single-occupied hole states $|a\sigma\rangle$, $|e_1\sigma\rangle$, $|e_2\sigma\rangle$. The single-particle hole excitations and local atomic states are shown in Fig. 5. The simplest way to describe the quasiparticle excitations between these states is to use the projective Hubbard X -operators that take the no-double occupancy constraint into account automatically³¹: $X_f^m \leftrightarrow X_f^{p,q} \equiv |p\rangle\langle q|$, where index $m \leftrightarrow (p, q)$ enumerates quasiparticles. There is a simple correspondence between the fermionic-like X -operators and single-electron creation-annihilation operators: $d_{f\alpha\sigma} = \sum_m \gamma_{\alpha\sigma}(m) X_f^m$, where $\gamma_{\alpha\sigma}(m)$ determines the partial weight of a quasiparticle m with spin σ and orbital index α . In these notations the Hamiltonian of the Hubbard model in the limit $U \rightarrow \infty$ has the form:

$$H = - \sum_{f,p} (\varepsilon^p - \mu) X_f^{p,p} - \sum_{f \neq g} \sum_{m,m'} t_{fg}^{mm'} X_f^{m\dagger} X_g^{m'}. \quad (3)$$

To study a quasiparticle energy spectrum of the system and its thermodynamics we use the Fourier transform of the two-time retarded Green function in the frequency representation, $G_{\alpha\sigma}(\mathbf{k}, E) \equiv \langle \langle d_{\mathbf{k}\alpha\sigma} | d_{\mathbf{k}\alpha\sigma}^\dagger \rangle \rangle_E$. This can be rewritten as: $G_{\alpha\sigma}(\mathbf{k}, E) = \sum_{m,m'} \gamma_{\alpha\sigma}(m) \gamma_{\beta\sigma}^*(m') D^{mm'}(\mathbf{k}, E)$, where $D^{mm'}(\mathbf{k}, E) = \langle \langle X_{\mathbf{k}}^m | X_{\mathbf{k}}^{m'\dagger} \rangle \rangle_E$ is the matrix Green function in the X -operators representation.

Using the diagram technique for Hubbard X -operators^{32,33} one obtains the generalized Dyson equation³⁴:

$$\hat{D}(\mathbf{k}, E) = \left[\hat{G}_0^{-1}(E) - \hat{P}(\mathbf{k}, E) \hat{t}_{\mathbf{k}} + \hat{\Sigma}(\mathbf{k}, E) \right]^{-1} \hat{P}(\mathbf{k}, E). \quad (4)$$

Here, $\hat{G}_0^{-1}(E)$ stands for the (exact) local Green function, $G_0^{mm'}(E) = \delta_{mm'} / [E - (\varepsilon_p - \varepsilon_q)]$. In the Hubbard-

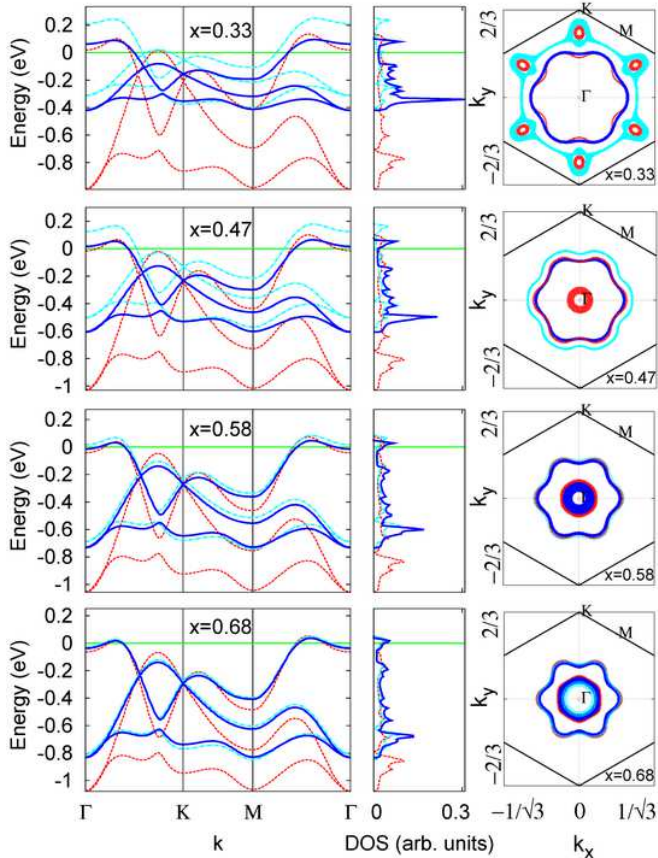


FIG. 6: (color online) Calculated band structure and the Fermi surface topology for Na_xCoO_2 for $x = 0.33, 0.47, 0.58, 0.68$. The dashed (red), solid (blue) and dash-dotted (cyan) curves represent the results of the rigid-band, the Gutzwiller, and the Hubbard-I approximations, respectively. The horizontal (green) line denotes the position of the chemical potential μ .

In the approximation the self-energy $\hat{\Sigma}(\mathbf{k}, E)$ is equal to zero and the strength operator $\hat{P}(\mathbf{k}, E)$ is replaced by the sum of the occupation factors, $P^{mm'}(\mathbf{k}, E) \rightarrow P^{mm'} = \delta_{mm'} \left[\langle X_f^{p,p} \rangle + \langle X_f^{q,q} \rangle \right]$, $m = m(p, q)$. Here ' $\langle \dots \rangle$ ' stands for the usual thermodynamic average. Thus, one obtains:

$$\hat{D}^{(0)}(\mathbf{k}, E) = \left[\hat{G}_0^{-1} - \hat{P} \hat{t}_\mathbf{k} \right]^{-1} \hat{P}. \quad (5)$$

In the paramagnetic phase the occupation factors are: $\langle X_f^{0,0} \rangle = x$, $\langle X_f^{a\sigma, a\sigma} \rangle = \frac{1-x}{2}$, $\langle X_f^{e_{1,2}\sigma, e_{1,2}\sigma} \rangle = 0$ which yields the diagonal form of the strength operator, $\hat{P} = \text{diag}(\frac{1+x}{2}, x, x)$. Therefore, the quasiparticle bands formed by the $a_{1g} \rightarrow a_{1g}$ hoppings will be renormalized by the $(1+x)/2$ factor, while the quasiparticle bands formed by the e_g' hopping elements will be renormalized by x .

In Fig. 6 the quasiparticle spectrum, the DOS, and the FS are displayed in different approximations. Within

Hubbard-I approximations one finds the narrowing of the bands with lowering the doping concentration x due to doping dependence of the quasiparticle's spectral weight introduced by the strength operator \hat{P} . However, the doping evolution of the FS is qualitatively similar to that in the rigid-band picture. Namely, the bandwidth reduction and the spectral weight renormalization do not change the topology of the FS. As a result, the presence of the strong electronic correlations within Hubbard-I approximation do not change qualitatively our results for the bare susceptibility. Quantitatively, the critical concentration x_m shifts towards higher values of the doping and becomes $x_m \approx 0.68$. The reason for this shift is the band narrowing and the renormalization of the quasiparticle's spectral weight, which enters the equation that determines the position of the chemical potential μ .

Luttinger's theorem, which holds for a perturbative expansion of the Green's function in terms of the interaction strength is violated within the Hubbard-I approximation. This violation is due to the renormalization of the spectral weight of the Green function by the occupation factors in the strength operator in Eq. (4). This is the reason why in spite of the e_g' band narrowing the e_g' hole pockets at the Fermi surface are still present at $x = 0.33$.

B. Gutzwiller approximation

The Gutzwiller approximation^{35,36,37} for the Hubbard model provides a good description for the correlated metallic system. Its multiband generalization was formulated in Ref.³⁸. In this approach, the Hamiltonian describing the interacting system far from the metal-insulator transition for $U \gg W$

$$H = H_0 + \sum_{f,\alpha} U_\alpha n_{f\alpha\uparrow} n_{f\alpha\downarrow}, \quad (6)$$

with H_0 being the free electron Hamiltonian (1), is replaced by the effective non-interacting Hamiltonian:

$$H_{\text{eff}} = - \sum_{f,\alpha,\sigma} (\varepsilon^\alpha + \delta\varepsilon^{\alpha\sigma} - \mu) n_{f\alpha\sigma} - \sum_{f \neq g, \sigma} \sum_{\alpha,\beta} \tilde{t}_{fg}^{\alpha\beta} d_{f\alpha\sigma}^\dagger d_{g\beta\sigma} + C. \quad (7)$$

Here, $\tilde{t}_{fg}^{\alpha\beta} = t_{fg}^{\alpha\beta} \sqrt{q_{\alpha\sigma}} \sqrt{q_{\beta\sigma}}$ is the renormalized hopping, $q_{\alpha\sigma} = \frac{x}{1-n_{\alpha\sigma}}$, $n_{\alpha\sigma} = \langle \Psi_0 | n_{f\alpha\sigma} | \Psi_0 \rangle \equiv \langle n_{f\alpha\sigma} \rangle_0$ is the orbital's filling factors, $x = 1 - \sum_{\alpha\sigma} n_{\alpha\sigma}$ is the equation for the chemical potential. $\delta\varepsilon^{\alpha\sigma}$ are the Lagrange multipliers yielding the correlation induced shifts of the single-electron energies. The constant C is determined from the condition that the ground state energy is the same for both Hamiltonians

$$\langle \Psi_0 | H_{\text{eff}} | \Psi_0 \rangle = \langle \Psi_g | H | \Psi_g \rangle, \quad (8)$$

where $|\Psi_0\rangle$ is the wave function of the free electron system (7), and $|\Psi_g\rangle$ is the Gutzwiller wave function for the Hamiltonian (6).

The Lagrange multipliers are determined by minimizing the energy,

$$\langle \Psi_0 | H_{eff} | \Psi_0 \rangle = - \sum_{\alpha, \sigma} (\varepsilon^\alpha + \delta\varepsilon^{\alpha\sigma} - \mu) \langle n_{f\alpha\sigma} \rangle_0 - \sum_{f \neq g, \sigma} \sum_{\alpha, \beta} \tilde{t}_{fg}^{\alpha\beta} \langle d_{f\alpha\sigma}^\dagger d_{g\beta\sigma} \rangle_0 + C, \quad (9)$$

with respect to the orbital filling factors $n_{\alpha\sigma}$. Here $C = \sum_{\alpha, \sigma} \delta\varepsilon^{\alpha\sigma} n_{\alpha\sigma}$, as determined from Eq. (8). This results in the following expression for the single-electron energy renormalizations:

$$\delta\varepsilon^{\alpha\sigma} = \frac{1}{2(1 - n_{\alpha\sigma})} \sum_{f \neq g, \sigma} \tilde{t}_{fg}^{\alpha\beta} \langle d_{f\alpha\sigma}^\dagger d_{g\beta\sigma} \rangle_0. \quad (10)$$

It is this energy shift that forces the e'_g FS hole pockets to sink below the Fermi energy¹⁶, which is clearly seen in the doping-dependent evolution of the quasiparticle dispersion and the FS as obtained within Gutzwiller approximation (Fig. 6). Although the narrowing of the bands due to strong correlations is similar to the one found in the Hubbard-I approximation, the FS obeys Luttinger's theorem. Note, in contrast to the Hubbard-I approximation the relative positions of the t_{2g} -bands are also renormalized by $\delta\varepsilon^{\alpha\sigma}$.

At the same time, for $x > 0.4$ the topology of the FS in the Gutzwiller approximation is qualitatively the same as in the rigid-band picture. The also yields similar results for the bare susceptibility's doping dependence discussed in Section III. The only effect of the strong correlations for χ_0 is the observed shift of the critical concentration towards higher values, $x_m \approx 0.6$. This is due to combined effect of the bands narrowing and the doping dependence of the a_{1g} and e'_g band's relative positions, determined by the Eq. (10).

Note, for $x < 0.4$, due to different FS topology that occurs in the Gutzwiller approximation, the bare susceptibility differs from that obtained in Ref.²⁹ where the strong renormalization of the electronic bands removing e'_g pockets away from the FS was neglected.

C. FLEX approximation

A certain disadvantage of the Gutzwiller and Hubbard-I like approximations is that the dynamic character of electronic correlations is not taken into account within these approaches. At the same time, the momentum and frequency dependencies of the self-energy $\Sigma(\mathbf{k}, \omega)$ play a crucial role, in particular, for determining the low-energies excitations close to the Fermi level. In this subsection we focus on the a_{1g} -band with nearest and next-nearest hopping integrals only and employ the single-band Fluctuation Exchange approximation (FLEX)³⁹

which sums all particle-hole(particle) ladder graphs for the generating functional self-consistently valid for the intermediate strength of the correlations. The FLEX equations for the single-particle Green function G , the self-energy Σ , the effective interaction V , the bare (χ^0) and renormalized spin (χ^s) and charge (χ^c) susceptibilities read

$$G_{\mathbf{k}}(\omega_n) = [\omega_n - \tau_{\mathbf{k}} + \mu - \Sigma_{\mathbf{k}}(\omega_n)]^{-1}, \quad (11)$$

$$\Sigma_{\mathbf{k}}(\omega_n) = \frac{T}{N} \sum_{\mathbf{p}, m} V_{\mathbf{k}-\mathbf{p}}(\omega_n - \omega_m) G_{\mathbf{p}}(\omega_m), \quad (12)$$

$$V_{\mathbf{q}}(\nu_m) = U^2 \left[\frac{3}{2} \chi_{\mathbf{q}}^s(\nu_m) + \frac{1}{2} \chi_{\mathbf{q}}^c(\nu_m) - \chi_{\mathbf{q}}^0(\nu_m) \right] \quad (13)$$

$$\chi_{\mathbf{q}}^0(\nu_m) = -\frac{T}{N} \sum_{\mathbf{k}, n} G_{\mathbf{k}+\mathbf{q}}(\omega_n + \nu_m) G_{\mathbf{k}}(\omega_n), \quad (14)$$

$$\chi_{\mathbf{q}}^{s,c}(\nu_m) = \frac{\chi_{\mathbf{q}}^0(\nu_m)}{1 \mp U \chi_{\mathbf{q}}^0(\nu_m)}, \quad (15)$$

where $\omega_n = i\pi T(2n + 1)$ and $\nu_m = i\pi T(2m)$. In the last equation the '-' sign in the denominator corresponds to the $\chi_{\mathbf{q}}^s(\nu_m)$, while the '+' sign corresponds to the $\chi_{\mathbf{q}}^c(\nu_m)$. We compute the Matsubara summations using 'almost real contour' technique of Ref.⁴⁰. I.e., the contour integrals are performed with a finite shift $i\gamma$ ($0 < \gamma < iT\pi/2$) into the upper half-plane. All final results are analytically continued from $\omega + i\gamma$ onto the real axis $\omega + i0^+$ by Padé approximation. The following results are based on FLEX solutions using a lattice of 64x64 sites with 4096 equidistant ω -points in the energy range of $[-30, 30]$. The temperature has been kept at $T = 0.05\tau$, where τ is the hopping amplitude to the nearest neighbors for the a_{1g} band corresponding to $t_1^{a_{1g}a_{1g}} = t_2^{a_{1g}a_{1g}} = t_3^{a_{1g}a_{1g}}$. The Hubbard repulsion was set to $U = 8\tau$.

Previously, the FLEX approximation has been applied successfully to the study of superconductivity as well as spin and charge excitations in Na_xCoO_2 ^{41,42}. Complementary, we will focus on the quasiparticle dispersion and study the impact of the momentum and frequency dependencies of the $\Sigma(\mathbf{k}, \omega)$, and the role played by the next-nearest hopping integral, τ' , corresponding to $t_4^{a_{1g}a_{1g}} = t_5^{a_{1g}a_{1g}} = t_6^{a_{1g}a_{1g}}$. The quasiparticle dispersion $E_{\mathbf{k}}$, which is determined from equation $E_{\mathbf{k}} - \tau_{\mathbf{k}} + \mu - \Sigma_{\mathbf{k}}(E_{\mathbf{k}}) = 0$, is shown in Fig. 7 for $\tau' = 0$ and $\tau' = -0.45$, in units of τ . First, observe that the local minimum around the Γ point appears only if the next-nearest-neighbor hopping τ' is included which agrees with our previous findings. In addition, we obtain a pronounced mass enhancement of the order of unity at the FS crossings - the so-called kink structure. This enhancement is due to low-energy spin fluctuations which are present in $\chi_{\mathbf{q}}^s(\omega)$ ⁴¹.

To shed more light onto the two-dimensional spin correlations, in Fig. 8 we display the static spin structure factor $\text{Re}\chi_{\mathbf{k}}^s(\omega = 0)$ from the FLEX for two different doping concentrations. As doping increases from $x = 0$ towards $x = 0.35$ the maximum in the spin susceptibility $\chi_{\mathbf{k}}^s(\omega = 0)$ moves towards the K-point of the first

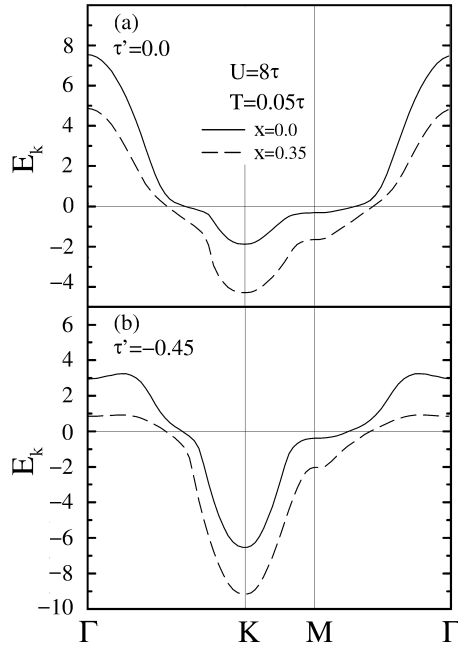


FIG. 7: Quasiparticle dispersion E_k (in units of τ , relative to μ) within FLEX approximation for (a) $\tau' = 0$ and (b) $\tau' = -0.45$ and for two doping concentrations.

BZ and develops into a sharp and commensurate peak at \mathbf{Q}_{AFM} and the incommensurate spin fluctuations are suppressed. One may also note that the commensurate peak is $\sim 60\%$ larger for $\tau' = -0.45$ than for $\tau' = 0$. These results are consistent with those obtained in a previous sections. We further notice smooth evolution of the quasiparticle dynamics with doping in Na_xCoO_2 showing no sign of unusual behavior at $x = 0$.

The frequency dependence of the imaginary part of the quasiparticle self-energy, i.e. $\text{Im}\Sigma_{\mathbf{k}}$, near the FS is shown in Fig. 9. We find the self-energy to be nearly isotropic along the FS with only a weak maximum occurring into the direction of the commensurate spin fluctuations. Near the Fermi energy the self-energy is clearly proportional to ω^2 at low energies for all dopings shown, which is indicative of the normal Fermi-liquid behavior. This is in sharp contrast to the FLEX analysis of the Hubbard model on the square lattice close to half-filling. There one typically finds 'marginal' Fermi-liquid behavior with $\text{Im}\Sigma_{\mathbf{k}} \approx \omega$ over a wide range of frequencies^{43,44}. Therefore, along this line one is tempted to conclude that the normal state of the superconducting cobaltates is more of conventional metallic nature than in the High- T_c cuprates. This is even more so, if one realizes from Fig. 9 that the quasiparticle scattering rate displays its smallest curvature for $x = 0.35$, which implies the quasiparticles to be rather well defined there. For lower x proximity of the FS to the van Hove singularity (see flat region of dispersion in Fig. 7) enhances both the absolute value of $\text{Im}\Sigma_{\mathbf{k}} \propto \omega$ as well as the curvature. This effect is most pronounced for $\tau' = 0$.

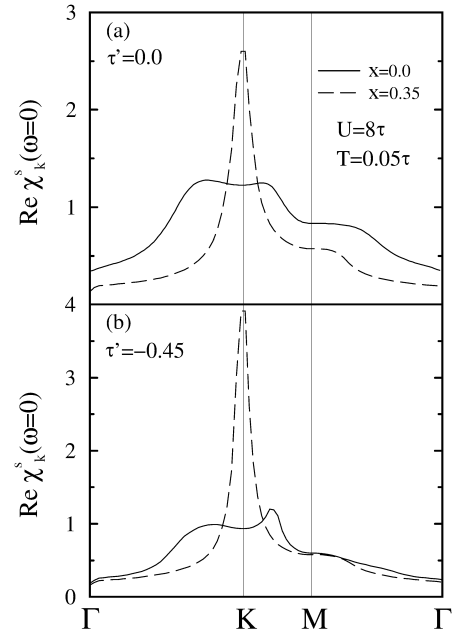


FIG. 8: Doping dependence of the static spin structure factor $\text{Re}\chi_{\mathbf{k}}^s(\omega = 0)$ for (a) $\tau' = 0$ and (b) $\tau' = -0.45$. Notice that for large $U = 8\tau$ the commensurate peak at K point is absent at a very low x .

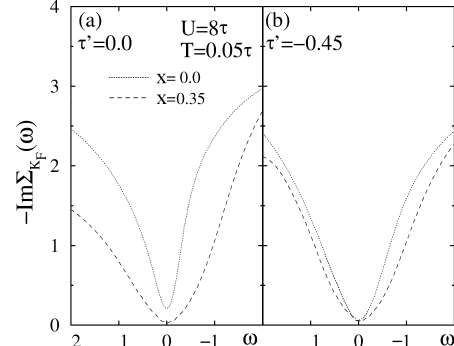


FIG. 9: Frequency dependence of quasiparticle self-energy $-\text{Im}\Sigma_{\mathbf{k}}(\omega)$ near the FS in direction $\Gamma - K$ for (a) $\tau' = 0$ and (b) $\tau' = -0.45$.

V. CONCLUSION

To conclude, we have calculated the doping dependent magnetic susceptibility in the tight-binding model with *ab-initio* calculated parameters. We find, that at a critical doping concentration, x_m , electron pocket develops on the FS in the center of the Brillouin zone. For $x < x_m$, the system shows a tendency towards an 120° AFM ordered state, while for $x > x_m$ a peak in the magnetic susceptibility forms at small wave vectors indicating a strong tendency towards an itinerant FS state. Within a tight-binding model we have estimated x_m to be approximately 0.56. Analyzing the influence of strong Coulomb repulsion and the corresponding reduction of the band-

width and the quasiparticle spectral weight in the strong-coupling Hubbard-I and Gutzwiller approximations, we have shown that the critical concentration changes to $x_m \approx 0.68$ and $x_m \approx 0.6$, respectively. At the same time, the underlying physics of the formation of the itinerant FM state remains the same.

We neglected the bonding-antibonding splitting due to the 3-dimensionality in the non-intercalated compounds. This splitting was taken into account in Ref.⁴¹, where within the FLEX approximation the single a_{1g} -band Hubbard model was considered. The results obtained also suggest a tendency to FM fluctuations for high doping concentrations. The presence of a local band minimum around the Γ point played a crucial role, similar to our present study.

To analyze the low-energy quasiparticle properties at low doping concentrations we have employed the single-band Hubbard model within the FLEX approximation. We have found a significant FS mass enhancement of order unity due to quasiparticle scattering from spin fluctuations. In contrast to the Hubbard model on the square lattice we have found the quasiparticle scattering rate to

display a conventional Fermi-liquid type of energy dependence. We have also shown that the static spin structure factor exhibits a large commensurate peak at wave vector \mathbf{Q}_{AFM} for doping concentrations of $x \approx 0.35$. This response was found to be significantly enhanced by the next-nearest-neighbor hopping, emphasizing its significance.

Acknowledgments

We would like to thank G. Bouzerar, P. Fulde, S.G. Ovchinnikov, N.B. Perkins, D. Singh, Ziqiang Wang, and V. Yushankhai for useful discussions, I. Mazin for critical reading of the manuscript, and S. Borisenko for sharing with us the experimental results prior to publication. M.M.K. acknowledge support from INTAS (YS Grant 05-109-4891) and RFBR (Grants 06-02-16100, 06-02-90537-BNTS). A.S. and V.I.A. acknowledge the financial support from RFBR (Grants 04-02-16096, 06-02-81017), and NWO (Grant 047.016.005).

* Electronic address: maxim@mpipks-dresden.mpg.de

- ¹ K. Takada, H. Sakurai, E. Takayama-Muromachi, F. Izumi, R.A. Dilanian, and T. Sasaki, *Nature* **422**, 53 (2003).
- ² I. Terasaki, Y. Sasago, and K. Uchinokura, *Phys. Rev. B* **56**, R12685 (1997).
- ³ Y. Wang, N. Rogado, R.J. Cava, and N.P. Ong, *Nature* **423**, 425 (2003).
- ⁴ M.L. Foo, Y. Wang, S. Watauchi, H.W. Zandbergen, T. He, R.J. Cava, and N.P. Ong, *Phys. Rev. Lett.* **92**, 247001 (2004).
- ⁵ B.C. Sales, R. Jin, K.A. Affholter, P. Khalifah, G.M. Veith, and D. Mandrus, *Phys. Rev. B* **70**, 174419 (2004).
- ⁶ D.J. Singh, *Phys. Rev. B* **61**, 13397 (2000).
- ⁷ K.-W. Lee, J. Kuneš, and W.E. Pickett, *Phys. Rev. B* **70**, 045104 (2004).
- ⁸ M.Z. Hasan, Y.-D. Chuang, D. Qian, Y.W. Li, Y. Kong, A. Kuprin, A.V. Fedorov, R. Kimmerling, E. Rotenberg, K. Rossnagel, Z. Hussain, H. Koh, N.S. Rogado, M.L. Foo, and R.J. Cava, *Phys. Rev. Lett.* **92**, 246402 (2004).
- ⁹ H.-B. Yang, S.-C. Wang, A.K.P. Sekharan, H. Matsui, S. Souma, T. Sato, T. Takahashi, T. Takeuchi, J.C. Campuzano, R. Jin, B.C. Sales, D. Mandrus, Z. Wang, and H. Ding, *Phys. Rev. Lett.* **92**, 246403 (2004).
- ¹⁰ H.-B. Yang, Z.-H. Pan, A.K.P. Sekharan, T. Sato, S. Souma, T. Takahashi, R. Jin, B.C. Sales, D. Mandrus, A.V. Fedorov, Z. Wang, and H. Ding, *Phys. Rev. Lett.* **95**, 146401 (2005).
- ¹¹ D. Qian, D. Hsieh, L. Wray, Y.-D. Chuang, A. Fedorov, D. Wu, J.L. Luo, N.L. Wang, L. Viciu, R.J. Cava, and M.Z. Hasan, *Phys. Rev. Lett.* **96**, 216405 (2006).
- ¹² L. Balicas, J.G. Analytis, Y.J. Jo, K. Storr, H. Zandbergen, Y. Xin, N.E. Hussey, F.C. Chou, and P.A. Lee, *Phys. Rev. Lett.* **97**, 126401 (2006).
- ¹³ D.J. Singh and D. Kasinathan, *Phys. Rev. Lett.* **97**, 016404 (2006).
- ¹⁴ P. Zhang, W. Luo, M.L. Cohen, and S.G. Louie, *Phys. Rev. Lett.* **93**, 236402 (2004).
- ¹⁵ H. Ishida, M.D. Johannes, and A. Liebsch, *Phys. Rev. Lett.* **94**, 196401 (2005).
- ¹⁶ S. Zhou, M. Gao, H. Ding, P.A. Lee, and Z. Wang, *Phys. Rev. Lett.* **94**, 206401 (2005).
- ¹⁷ D.J. Singh, *Phys. Rev. B* **68**, 020503(R) (2003).
- ¹⁸ A.T. Boothroyd, R. Coldea, D.A. Tennant, D. Prabhakaran, L.M. Helme, and C.D. Frost, *Phys. Rev. Lett.* **92**, 197201 (2004).
- ¹⁹ S.P. Bayrakci, I. Mirebeau, P. Bourges, Y. Sidis, M. Endlerle, J. Mesot, D.P. Chen, C.T. Lin, and B. Keimer, *Phys. Rev. Lett.* **94**, 157205 (2005).
- ²⁰ L.M. Helme, A.T. Boothroyd, R. Coldea, D. Prabhakaran, D.A. Tennant, A. Hiess, and J. Kulda, *Phys. Rev. Lett.* **94**, 157206 (2005).
- ²¹ W. Kohn and L.J. Sham, *Phys. Rev. A* **140**, 1133 (1965).
- ²² O.K. Andersen and O. Jepsen, *Phys. Rev. Lett.* **53**, 2571 (1984).
- ²³ J.D. Jorgensen, M. Avdeev, D.G. Hinks, J.C. Burley, and S. Short, *Phys. Rev. B* **68**, 214517 (2003).
- ²⁴ N. Marzari and D. Vanderbilt, *Phys. Rev. B* **56**, 12847 (1997).
- ²⁵ V.I. Anisimov, D.E. Kondakov, A.V. Kozhevnikov, I.A. Nekrasov, Z.V. Pchelkina, J.W. Allen, S.-K. Mo, H.-D. Kim, P. Metcalf, S. Suga, A. Sekiyama, G. Keller, I. Leonov, X. Ren, and D. Vollhardt, *Phys. Rev. B* **71**, 125119 (2005).
- ²⁶ M.D. Johannes, D.A. Papaconstantopoulos, D.J. Singh, and M.J. Mehl, *Europhys. Lett.* **68**, 433 (2004).
- ²⁷ K. Kuroki, S. Onari, Y. Tanaka, R. Arita, and T. Nojima, *Phys. Rev. B* **73**, 184503 (2006).
- ²⁸ S. Borisenko, private communication.
- ²⁹ M.D. Johannes, I.I. Mazin, D.J. Singh, and D.A. Papacon-

stantopoulos, Phys. Rev. Lett. **93**, 097005 (2004).

³⁰ M. Indergand, Y. Yamashita, H. Kusunose, and M. Sigrist, Phys. Rev. B **71**, 214414 (2005).

³¹ J.C. Hubbard, Proc. Roy. Soc. London A **277**, 237 (1964).

³² R.O. Zaitsev, Sov. Phys. JETP **41**, 100 (1975).

³³ Yu. Izumov and B.M. Letfulov, J. Phys.: Condens. Matter **3**, 5373 (1991).

³⁴ S.G. Ovchinnikov and V.V. Val'kov, *Hubbard Operators in the Theory of Strongly Correlated Electrons* (Imperial College Press, London, 2004).

³⁵ M.C. Gutzwiller, Phys. Rev. Lett. **10**, 159 (1963); Phys. Rev. B **134A**, 923 (1964); Phys. Rev. B **137A**, 1726 (1965).

³⁶ F. Gebhard, Phys. Rev. B **41**, 9452 (1990).

³⁷ G. Kotliar and A.E. Ruckenstein, Phys. Rev. Lett. **57**, 1362 (1986).

³⁸ J. Bünnemann, F. Gebhard, and W. Weber, J. Phys.: Condens. Matter **9**, 7343 (1997).

³⁹ N.E. Bickers, D.J. Scalapino, and S.R. White, Phys. Rev. Lett. **62**, 961 (1989); J. Altman, W. Brenig, and A.P. Kampf, Eur. Phys. J. B **18**, 429 (2000).

⁴⁰ J. Schmalian, M. Langer, S. Grabowski, and K.H. Bennemann, Computer Phys. Comm. **93**, 141 (1996).

⁴¹ K. Kuroki, S. Ohkubo, T. Nojima, R. Arita, S. Onari, and Y. Tanaka, cond-mat/0610494 (unpublished); K. Kuroki, S. Onari, Y. Tanaka, R. Arita, and T. Nojima, Phys. Rev. B **73**, 184503 (2006).

⁴² Y. Yanase, M. Mochizuki, and M. Ogata, J. Phys. Soc. Jpn. **74**, 2568 (2005), *ibid.* 3351 (2005).

⁴³ J. Altman, W. Brenig, and A.P. Kampf, Eur. Phys. J. B **18**, 429 (2000).

⁴⁴ S. Wermbter, Phys. Rev. B **55**, R10149 (1997).